

# Frequency-domain theory of Compton Scattering by a bound electron

Shang Shi<sup>1,7</sup>, Jing Chen<sup>2,3</sup>, Yu-Jun Yang<sup>4</sup>, Zong-Chao Yan<sup>5,6</sup>, Xiao-Jun Liu<sup>6</sup> and Bingbing Wang<sup>1,7\*</sup>

<sup>1</sup>Laboratory of Optical Physics, Beijing National Laboratory for Condensed Matter Physics, Institute of Physics, Chinese Academy of Sciences, Beijing 100190, China

<sup>2</sup>HEDPS, Center for Applied Physics and Technology, Peking University, Beijing 100871, China

<sup>3</sup>Institute of Applied Physics and Computational Mathematics, Beijing 100088, China

<sup>4</sup>Institute of Atomic and Molecular Physics, Jilin University, Changchun 130012, China

<sup>5</sup>Department of Physics, University of New Brunswick, Fredericton, New Brunswick, E3B 5A3, Canada

<sup>6</sup>State Key Laboratory of Magnetic Resonance and Atomic and Molecular Physics,

Wuhan Institute of Physics and Mathematics, Innovation Academy for Precision Measurement Science and Technology, Chinese Academy of Sciences, Wuhan 430071, China and

<sup>7</sup>University of Chinese Academy of Sciences, Beijing 100049, China

(Dated: February 26, 2021)

We have developed a frequency-domain formulation based on the nonperturbative quantum electrodynamic to study nonlinear Compton scattering of two photons off a bound electron inside an atom in a strong X-ray laser field. In contrast to previous theoretical works, our results clearly reveal the existence of anomalous redshift phenomenon observed experimentally by Fuchs *et al.* [Nat. Phys. **11**, 964 (2015)] and suggest its origin as the binding energy of the electron as well as the momentum transfer from incident photons to the electron during the scattering process. Our work builds a bridge between intense-laser atomic physics and Compton scattering process that can be used to study atomic structure and dynamics at high laser intensities.

With the first use of the Linac Coherent Light Source at the SLAC National Accelerator Laboratory in 2010 [1], the era of exploring the nonlinear interaction of ultrafast and ultra-intense X-rays with matters has begun. By using X-ray free electron lasers [2–6], people have observed for the first time extensive nonlinear phenomena at X-ray wavelengths, including the X-ray second harmonic generation in diamonds [7], two-photon absorption in the hard X-ray region [8, 9], electron femtosecond response to an ultra-intense X-ray radiation [10], and nonlinear Compton scattering (NCS) of X-ray photons [11]. Among them, the NCS is a particularly interesting phenomenon because the observed anomalous redshift of the scattered photon can be regarded as a breakdown of the widely-used free-electron approximation for bound electrons [12–22].

As far as we know, there exist a few theoretical studies devoted to the NCS processes involving bound electrons. Hopersky *et al.* [23] first studied the Compton scattering of two X-ray photons by helium atom using second-order perturbation theory in dipole approximation. However, their prediction of the emission spectrum showed an oscillating structure that has not been observed experimentally. Recently, Krebs *et al.* [24] developed a nonperturbative approach based on the time-dependent Schrödinger equation to investigate linear and nonlinear Compton scatterings of X-ray photons by atoms. However, their results were consistent with the predictions of the free-electron model and do not support the existence of the redshift found in [11]. More recently, Venkatesh and Robicheaux [25] even claimed that their theoretical results exhibit a blueshift compared with the scattered photon energy predicted by the free-electron model during an NCS process. Therefore, the origin of the anomalous redshift phenomenon observed by Fuchs *et al.* [11] is still an open question.

Motivated by the theoretical gap of the NCS mechanism, in this work we will apply the nonperturbative quantum electrodynamic (QED) frequency domain theory to study the NCS process of bound electrons. This theory has previously been successfully applied to recollision processes in strong laser fields [26–29]. The advantages of the QED method in treating the Compton scattering could be shortly provided. Specifically, we will focus on the double differential probability (DDP) for the Compton scattering process of a bound electron in an X-ray laser field. Our calculation will clearly demonstrate that in the DDP spectrum of the two-photon NCS, as the energy of the scattered photon increases, a redshift peak will appear, which is in sharp contrast to the free-electron results [30–32], and other theoretical predictions [24, 25]. Our theoretical results can be considered as the first qualitative confirmation of the measurement of Fuchs *et al.* [11].

In the following, natural units ( $\hbar = c = 1$ ) are used throughout unless otherwise stated. Since a Compton scattering involves incident and scattered photons of different frequencies, the quantum system consists of an atom and two linearly polarized radiation fields with their corresponding vector potentials  $\mathbf{A}_1(\mathbf{r})$  and  $\mathbf{A}_2(\mathbf{r})$ , where  $\mathbf{A}_1(\mathbf{r})$  coincides with the incident X-ray laser field of frequency  $\omega_1$  and wave vector  $\mathbf{k}_1$ , and  $\mathbf{A}_2(\mathbf{r})$  with the scattered photon field of frequency  $\omega_2$  and wave vector  $\mathbf{k}_2$ . The Hamiltonian of this atom-radiation system is thus

$$H = H_0 + U + V. \quad (1)$$

In the above,

$$H_0 = \frac{(-i\nabla)^2}{2m} + \omega_1 N_{a_1} + \omega_2 N_{a_2} \quad (2)$$

is the non-interaction part of the Hamiltonian, where  $N_{a_1} = (a_1^\dagger a_1 + a_1 a_1^\dagger)/2$  and  $N_{a_2} = (a_2^\dagger a_2 + a_2 a_2^\dagger)/2$  are the number operators of the incident and the scattered photons, respec-

\* wbb@aphy.iphy.ac.cn

tively, with  $a_i(a_i^\dagger)$  being the annihilation (creation) operator for  $i = 1, 2$ ;  $U$  is the atomic binding potential; and  $V$  is the total electron-photon interaction potential that can be written as  $V = V_1 + V_{21} + V_{22}$  with

$$V_1 = \frac{e\mathbf{A}_1(\mathbf{r}) \cdot (-i\nabla)}{m} + \frac{e^2\mathbf{A}_1^2(\mathbf{r})}{2m} \quad (3)$$

$$V_{21} = \frac{e^2\mathbf{A}_1(\mathbf{r}) \cdot \mathbf{A}_2(\mathbf{r})}{m} \quad (4)$$

and

$$V_{22} = \frac{e\mathbf{A}_2(\mathbf{r}) \cdot (-i\nabla)}{m}. \quad (5)$$

Here, we have neglected the term  $\frac{e^2\mathbf{A}_2^2(\mathbf{r})}{2m}$  for its weak strength. The vector potentials of the incident and scattered photon modes are  $\mathbf{A}_1(\mathbf{r}) = g_1(\epsilon_1 a_1 e^{i\mathbf{k}_1 \cdot \mathbf{r}} + \text{c.c.})$  and  $\mathbf{A}_2(\mathbf{r}) = g_2(\epsilon_2 a_2 e^{i\mathbf{k}_2 \cdot \mathbf{r}} + \text{c.c.})$ , where  $g_1 = (2\omega_1 V_\gamma)^{-\frac{1}{2}}$  and  $g_2 = (2\omega_2 V'_\gamma)^{-\frac{1}{2}}$  with  $V_\gamma$  and  $V'_\gamma$  the normalization volumes of the photon modes, and  $\epsilon_1$  and  $\epsilon_2$  are the corresponding polarization vectors. According to the experimental set-up in Ref. [11], the polarization and wave vectors of the incident laser field are chosen along the  $x$ - and  $z$ -axis, respectively, while the direction of  $\mathbf{k}_2$  is characterized by the spherical coordinates  $(\theta, \phi)$ .

In the frequency-domain theory, since the atom-laser system is regarded as an isolated one, the total energy of the system is conserved throughout the transition process and hence the formal scattering theory [33] can be applied. The  $S$ -matrix element between the initial state  $|\psi_i\rangle$  and the final state  $|\psi_f\rangle$  is

$$S_{fi} = \langle \psi_f^- | \psi_i^+ \rangle, \quad (6)$$

where

$$\psi_j^\pm = \psi_j + \frac{1}{E_j - H \pm i\epsilon} V \psi_j^\pm \quad (7)$$

with  $j$  taken to be  $i$  or  $f$ . Physically,  $\psi_i^+$  is the scattering state at  $t = 0$  which has developed from a pre-collision state  $\psi_i$  in the remote past, whereas  $\psi_f^-$  is the scattering state at  $t = 0$  which will develop to a post-collision state  $\psi_f$  in the remote future. After some algebraic manipulation, the  $S$ -matrix element can be recast into

$$S_{fi} = \delta_{fi} - 2\pi i \delta(E_f - E_i) T_{fi}, \quad (8)$$

where

$$T_{fi} = \langle \psi_f | V | \psi_i \rangle + \langle \psi_f | V \frac{1}{E_i - H_0 - U - V + i\epsilon} V | \psi_i \rangle \quad (9)$$

is the  $T$ -matrix element. The first term in Eq. (9) corresponds to a one-step transition and the second term corresponds to a two-step transition. The normal Compton scattering is a one-step transition. For an NCS, in principle, both transition processes should be taken into account. However, since the contribution of the two-step transition is much smaller than that

of the one-step process under the present laser conditions, the second term in Eq. (9) can be dropped. Hence, the  $T$ -matrix element for an NSC can be expressed as

$$T_{fi} = T_{AP} + T_{AA-} + T_{AA+}, \quad (10)$$

where  $T_{AP} = \langle \psi_f | V_{22} | \psi_i \rangle$ ,  $T_{AA-} = \langle \psi_f | V_{21-} | \psi_i \rangle$ , and  $T_{AA+} = \langle \psi_f | V_{21+} | \psi_i \rangle$  with  $V_{22} = \frac{e}{m} g_2 e^{-i\mathbf{k}_2 \cdot \mathbf{r}} a_2^\dagger \epsilon_2^* \cdot (-i\nabla)$ ,  $V_{21-} = \frac{e^2}{m} g_1 g_2 \epsilon_2^* \cdot \epsilon_1 e^{i(\mathbf{k}_1 - \mathbf{k}_2) \cdot \mathbf{r}} a_1 a_2^\dagger$ , and  $V_{21+} = \frac{e^2}{m} g_1 g_2 \epsilon_2^* \cdot \epsilon_1^* e^{-i(\mathbf{k}_1 + \mathbf{k}_2) \cdot \mathbf{r}} a_1^\dagger a_2^\dagger$ . Figure 1 illustrates the corresponding schematic diagrams of these three processes, in which we call  $T_{AP}$  the laser-assisted electron-mode (LEM) transition shown in Fig. 1(a), and call  $T_{AA\pm}$  the electron-assisted mode-mode (EMM) transition shown in Fig. 1(b) and (c) respectively. The LEM transition describes the process where the bound electron is ionized after absorbing several photons from the laser field, and at the same time, a photon of frequency  $\omega_2$  is scattered, whereas the EMM transition describes a similar process except that a second photon of frequency  $\omega_1$  is either absorbed or emitted.

In Eq. (10),  $|\psi_i\rangle = \Phi_i(\mathbf{r}) \otimes |l\rangle \otimes |0\rangle$  is the initial state of the scattering system, i.e., the eigenstate of the Hamiltonian operator  $H_0 + U(\mathbf{r})$  with the corresponding eigenvalue  $E_i = (-E_B) + (l + \frac{1}{2})\omega_1 + \frac{1}{2}\omega_2$ , where  $\Phi_i(\mathbf{r})$  is the ground-state wave function of the atomic electron with the binding energy  $E_B > 0$ , and  $|l\rangle$  and  $|0\rangle$  are the Fock states of the incident and scattered photons with photon number  $l$  and 0 respectively. Also in Eq. (10),  $|\psi_f\rangle = \Psi_{\mathbf{P}_f n_f} \otimes |1\rangle$  is the final state of the system with energy  $E_f = \mathbf{P}_f^2 / (2m) + (n_f + \frac{1}{2} + u_p)\omega_1 + \frac{3}{2}\omega_2$ , where  $\mathbf{P}_f$  is the final momentum of the electron along the direction of  $(\theta_f, \phi_f)$ ,  $u_p$  is the ponderomotive energy in unit of the incident photon energy, and  $\Psi_{\mathbf{P}_f n_f}$  is the Volkov state of the electron in the quantum laser field given by [26]

$$\Psi_{\mathbf{P}_f n_f} = V_e^{-1/2} \sum_{j=-n_f}^{\infty} e^{i[\mathbf{P}_f + (u_p - j)\mathbf{k}_1] \cdot \mathbf{r}} \mathcal{J}_j(\zeta, \eta)^* |n_f + j\rangle. \quad (11)$$

In the above,

$$\mathcal{J}_j(\zeta, \eta) = \sum_{m=-\infty}^{\infty} J_{-j-2m}(\zeta) J_m(\eta), \quad (12)$$

is the generalized Bessel function,  $\zeta = 2\alpha \sqrt{u_p} \mathbf{P}_f \cdot \epsilon_1$ ,  $\eta = u_p/2$ ,  $\alpha \approx 1/137$  is the fine-structure constant, and  $V_e$  is the normalization volume of the electron.

The matrix element of the LEM transition  $T_{AP}$  can be written as

$$T_{AP} = \frac{e}{m} V_e^{-1/2} g_2 \epsilon_2^* \cdot [\mathbf{P}_f + (u_p - q)\mathbf{k}_1] \mathcal{J}_q(\zeta, \eta) \times \Phi_i(\mathbf{P}_f + \mathbf{k}_2 + (u_p - q)\mathbf{k}_1), \quad (13)$$

where  $q = l - n_f$  denotes the number of photons transferred from the incident laser field during the NCS process. For the case of two-photon NCS,  $q = 2$ . The matrix elements of the

EMM transitions  $T_{AA\pm}$  are given by

$$T_{AA-} = \frac{e^2}{m} V_e^{-1/2} \Lambda g_2 \boldsymbol{\epsilon}_1 \cdot \boldsymbol{\epsilon}_2^* \mathcal{J}_{q-1}(\zeta, \eta) \times \Phi_i(\mathbf{P}_f + \mathbf{k}_2 + (u_p - q)\mathbf{k}_1) \quad (14)$$

and

$$T_{AA+} = \frac{e^2}{m} V_e^{-1/2} \Lambda g_2 \boldsymbol{\epsilon}_1^* \cdot \boldsymbol{\epsilon}_2^* \mathcal{J}_{q+1}(\zeta, \eta) \times \Phi_i(\mathbf{P}_f + \mathbf{k}_2 + (u_p - q)\mathbf{k}_1), \quad (15)$$

where  $\Lambda = \sqrt{u_p}/(ae)$  represents the half amplitude of the classical field in the limits of  $g_1 \rightarrow 0$  and  $l \rightarrow \infty$ . Since the contribution of  $T_{AA+}$  is much smaller than that of the other two terms, it is ignored under our laser conditions.

The expression of the DDP for a Compton scattering process can be written as [34]

$$\frac{dW_{i \rightarrow f}}{d\omega_2 d\Omega} = \int 2\pi |T_{fi}|^2 \delta(E_i - E_f) \frac{V'_\gamma}{(2\pi)^3} \frac{V_e}{(2\pi)^3} \omega_2^2 d^3 P_f, \quad (16)$$

where  $d\Omega$  is the differential solid angle of vector  $\mathbf{k}_2$ . We now calculate the DDP for the two-photon Compton scattering by a  $1s$  electron of Be atom, where the intensity of the laser field is  $4 \times 10^{20}$  W/cm<sup>2</sup> and the photon energy is 9.25 keV. Figure 2 presents the DDP of the NCS at the scattering angles of  $95^\circ$  (a) and  $150^\circ$  (b), where the wave vector of the scattered photon  $\mathbf{k}_2$  is fixed in the polarization plane of the incident laser field defined by  $\mathbf{k}_1$  and  $\boldsymbol{\epsilon}_1$ , i.e., the azimuthal angle  $\phi = 0^\circ$ . In Fig. 2(a)-(b), the vertical lines indicate the scattered photon energy predicted by the free-electron model [35]:

$$\omega_2 = \frac{q\omega_1}{1 + \frac{q\omega_1}{m}(1 - \cos\theta)}. \quad (17)$$

It can be clearly seen from Fig. 2 that under these scattering angles, the peak positions of the scattered spectra are always red shifted with respect to the one given by the free-electron model, which confirms the experimental observation in [11]. The redshift value of the scattered photon energy is about 500 eV for  $\theta = 95^\circ$  and 580 eV for  $\theta = 150^\circ$ , which are much larger than the binding energy of the  $1s$  electron in Be atom.

From Eq. (10), the total DDP can be classified into two parts: the contributions by LEM and EMM. In order to find

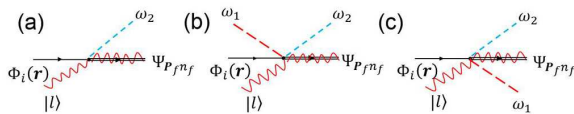


FIG. 1. Schematic for the one-step transition of Compton scattering by a bound electron. The single straight line represents the bound electron state, the wavy line represents the Fock state of the incident laser, the combination of wavy and double lines represents the Volkov state, the red and blue dashed lines represent the scattered photons of frequency  $\omega_1$  and  $\omega_2$  respectively, and the vertex denotes the transition operator  $V_{22}$  in (a),  $V_{21-}$  in (b), and  $V_{21+}$  in (c).

out the origin of the redshift, we calculate them separately according to Eqs. (13) and (14), and the results are indicated by the blue dotted lines (LEM) and pink short-dashed lines (EMM) in Fig. 2(a)-(b). One can see that the distribution of the total DDP is dominated by LEM at  $\theta = 95^\circ$  and is dominated by EMM at  $\theta = 150^\circ$ . Furthermore, under the present laser conditions, we find that both parameters  $\zeta$  and  $\eta$  are much smaller than 1 and hence the generalized Bessel functions in Eqs. (13)-(14) can be replaced by  $J_{-1}(\eta) \approx C_1$  and  $\mathcal{J}_1(\zeta, \eta) \approx -\zeta/2 \approx C_2 \mathbf{P}_f \cdot \boldsymbol{\epsilon}_1$ , where  $C_1$  and  $C_2$  are two constants. Thus, the matrix element of LEM transition can be approximated as

$$T_{AP} \approx C_1 \frac{e}{m} V_e^{-1/2} g_2 [P_f \cos \theta_{e_2} + (u_p - q)\mathbf{k}_1 \cdot \boldsymbol{\epsilon}_2^*] \times \Phi_i(\mathbf{P}_f + \mathbf{k}_2 + (u_p - q)\mathbf{k}_1) \quad (18)$$

with  $\theta_{e_2}$  being the angle between  $\boldsymbol{\epsilon}_2^*$  and the electron momentum  $\mathbf{P}_f$ , and the matrix element of EMM transition can be approximated as

$$T_{AA-} \approx C_2 \frac{e^2}{m} V_e^{-1/2} \Lambda g_2 \boldsymbol{\epsilon}_1 \cdot \boldsymbol{\epsilon}_2^* P_f \cos \theta_{e_1} \times \Phi_i(\mathbf{P}_f + \mathbf{k}_2 + (u_p - q)\mathbf{k}_1) \quad (19)$$

with  $\theta_{e_1}$  being the angle between  $\boldsymbol{\epsilon}_1$  and the electron momentum  $\mathbf{P}_f$ . Substituting Eqs. (18) and (19) into Eq. (16) yields almost the same results as the DDP with no approximation, as shown by the triangles and circles in Fig. 2(a)-(b). From Eqs. (18) and (19), one can find that, for a certain geometry among the three vectors  $\mathbf{k}_1$ ,  $\mathbf{k}_2$ , and  $\mathbf{P}_f$ , both equations depend on the value of the electron momentum and the wavefunction of Be atom  $\Phi_i(\mathbf{P}_f + \mathbf{k}_2 + (u_p - q)\mathbf{k}_1)$ . In order to investigate the influence of this wavefunction on the distribution of DDP, we integrate its modulus squared over the final electron momentum  $\mathbf{P}_f$  and obtain the angle-resolved energy spectrum, as shown in Fig. 2(c). It can be found that the peaks shown by dots in the spectrum of Fig. 2(c) are always redshifted relative to the free-electron model shown by the solid line in Fig. 2(c), and these redshifts are smaller than 280 eV. It indicates that a redshift can be triggered by the bound electron in NCS, but is still much smaller than the redshifts shown in Fig. 2(a) and (b). Furthermore, by analyzing the terms in Eqs. (18) and (19), we find that the total DDP linearly depends on the value of the ionized electron momentum  $P_f$ . In particular, the value of  $P_f$  and thus the total DDP decrease as the scattered photon energy increases due to the energy conservation. As a result, an obvious redshift of the DDP spectrum is formed, which is mainly caused by the dependence of DDP on the ionized electron momentum and bound-state wavefunction.

We now qualitatively compare our NCS spectra with the experimental results observed in [11] by using a magnification factor  $\delta$ , where the DDP of two-photon NCS is shown in Fig. 3 at  $\theta = 103^\circ$  for  $\delta = 5.55 \times 10^{11}$  (a) and  $\theta = 131^\circ$  for  $\delta = 3.88 \times 10^{11}$  (b). In Fig. 3(a)-(b), the lines and geometric symbols represent, respectively, the theoretical and experimental results under various intensities. As shown in Fig. 3(a) and (b), the peaks of our theoretical curves agree well with the experimental results, which are the second-order effects of

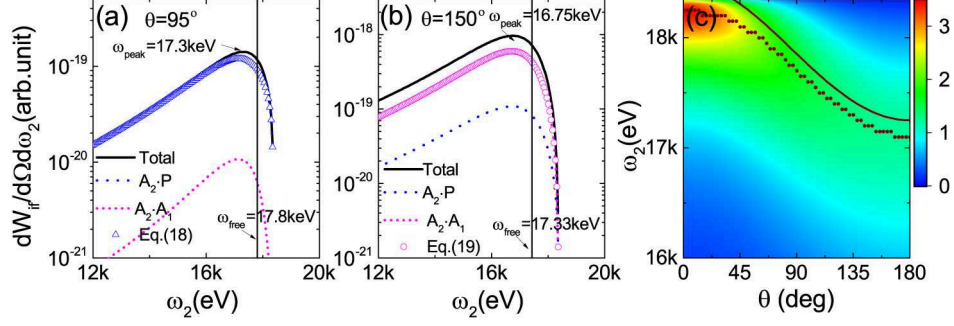


FIG. 2. The DDP for two-photon NCS by atomic Be as a function of the scattered photon energy  $\omega_2$  at the scattering angle of  $\theta = 95^\circ$  (a),  $\theta = 150^\circ$  (b). The black solid, blue dotted lines and pink short-dashed lines represent the total DDP, the DDP by LEM (Eq. (13)) and the DDP by EMM (Eq. (14)), respectively. The blue triangles are for the DDP by Eq. (18) and the pink circles the DDP by Eq. (19). The vertical lines are  $\omega_2$  predicted by Eq. (17). The scattered wave vector  $\mathbf{k}_2$  is fixed in the polarization plane defined by  $\mathbf{k}_1$  and  $\boldsymbol{\epsilon}_1$ . The integral of  $|\Phi_i(\mathbf{P}_f + \mathbf{k}_2 + (u_p - q)\mathbf{k}_1)|^2$  over  $\mathbf{P}_f$  as a function of  $\omega_2$  and  $\theta$  is shown in (c), where the dots represent the scattered photon energy corresponding to the peaks at different scattering angles and the solid line represents the prediction by Eq. (17).

laser intensity.

By integrating the DDP over the scattered photon energy, we obtain the corresponding single differential probability (SDP) shown in Fig. 3 with  $\delta = 3.11 \times 10^9$  for the case of  $\omega_1 = 8.84 \text{ keV}$  (c) and  $\omega_1 = 9.75 \text{ keV}$  (d). It shows that the SDP increases as the scattering angle increases, which is in agreement with the experimental results displayed by the red stars in the graphs. Moreover, the total SDP also includes two parts: the contributions from EMM and LEM. One may find that the contribution from LEM transition is insensitive to the scattering angle, whereas the contribution from EMM transi-

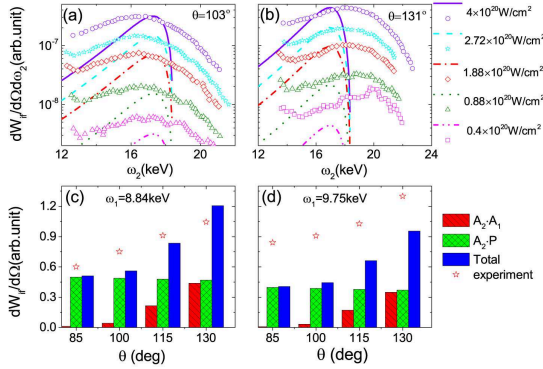


FIG. 3. (a)-(b) Comparison of the DDP for two-photon NCS by Be between theory and experiment at  $\theta = 103^\circ$  (a) and  $\theta = 131^\circ$  (b). The lines and geometric figures represent, respectively, the theoretical and experimental values under different laser intensities. The incident photon energy  $\omega_1$  is 9.25 keV. (c)-(d) Comparison of SDP between theory and experiment at different scattering angles for  $\omega_1 = 8.84 \text{ keV}$  (c) and  $\omega_1 = 9.75 \text{ keV}$  (d). The stars represent the experimental data points. Note: the theoretical values in the same graph are magnified by the same multiple.

tion increases with the scattering angle. Thus, as the scattering angle increases, the EMM transition will become more important in SDP.

In order to present the spectra distribution of the two-photon NCS more comprehensively, the angle-resolved energy spectra of the scattered light are shown in Fig. 4 at  $\phi = 0^\circ$  (a)-(c) and  $\phi = 45^\circ$  (d)-(f), where the laser parameters are the same as those in Fig. 2. The solid lines in Fig. 4(a) and (d) represent the values of the scattered photon energy, predicted by the free-electron model Eq. (17), and the dots represent the scattered photon energies corresponding to the maximum values of the DDP. It can be seen that these photon energies calculated by our theory are always redshifted, relative to the values of the free-electron model for the whole range of the

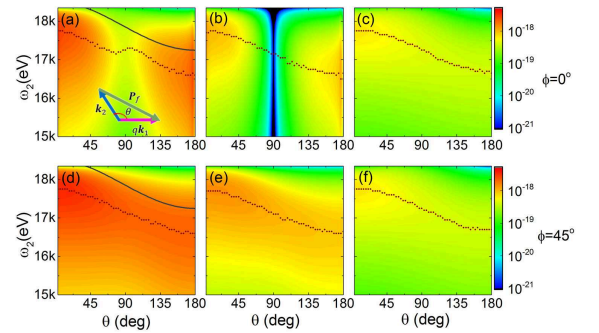


FIG. 4. The DDP for two-photon NCS by Be as a function of the scattering angle  $\theta$  and the scattered photon energy  $\omega_2$  for the case of  $\phi = 0^\circ$  (a)-(c) and  $\phi = 45^\circ$  (d)-(f), where the graphs in the left, middle, and right column shows, respectively, the total DDP, the DDP due to EMM, and the DDP due to LEM. The black lines represent  $\omega_2$  determined by Eq. (17), and the red dots represent  $\omega_2$  corresponding to the peaks at different scattering angles.

scattering angle. Although the forward scattering is not given in Fuchs *et al.* work [11], our results show that the redshift still exists significantly in the forward scattering. In addition, with the increase of the scattering angle, the peak energy of the NCS spectra decreases gradually, which is similar to the prediction of the free-electron model. It can be attributed to the relationship between the density distribution of the wavefunction and the angle  $\theta$  shown in Fig. 2(c). By analyzing the argument of the wavefunction, we can understand directly from the inset of Fig. 4(a) that, with  $u_p$  neglected, the peak of DDP occurs at about the momentum transfer  $\mathbf{P}_f = q\mathbf{k}_1 - \mathbf{k}_2$ . Since this momentum transfer increases with the scattering angle, according to the conservation of energy in the NCS process, the electron energy gained from the scattering must increase, resulting in a decrease in the energy of the scattered photon.

The spectra shown in Fig. 4(b) and (e) are the DDP contributed by EMM transition, and that by the LEM transition is shown in Fig. 4(c) and (f). One can see from Fig. 4(b) and (e) that the DDP of EMM transition obviously depends on the azimuthal angle  $\phi$  of the scattered wave vector; whereas the DDP of LEM transition is almost independent of the azimuthal angle, as shown in Fig. 4(c) and (f). Thus, for  $\phi = 0^\circ$ , the DDP has a minimum around  $\theta = 90^\circ$ , which can be explained as follows. Since in this case  $\mathbf{k}_2 \perp \mathbf{k}_1$  and  $\mathbf{k}_2 \parallel \boldsymbol{\epsilon}_1$ , we then have  $\boldsymbol{\epsilon}_2 \perp \boldsymbol{\epsilon}_1$ . As a result, the probability contributed by EMM transition becomes zero at  $\theta = 90^\circ$  because it is proportional to  $\boldsymbol{\epsilon}_1 \cdot \boldsymbol{\epsilon}_2^*$ . Moreover, comparing the contributions from EMM and LEM transitions under different azimuthal angles,

the LEM transition dominates the two-photon NCS process as the polarization directions of the incident and the scattered lights tend to be perpendicular with each other, i.e.,  $\boldsymbol{\epsilon}_2 \perp \boldsymbol{\epsilon}_1$  and  $\mathbf{k}_2 \perp \mathbf{k}_1$ , whereas the EMM transition dominates the two-photon NCS process for all other scattering geometries.

In conclusion, we have extended the frequency-domain theory based on the nonperturbative QED to investigate the NCS of two X-ray photons by an atom. Our theoretical results are in qualitative agreement with the experimental results of Ref. [11] and thus clarify the underlying physical mechanism for the nonlinear scattering process, i.e., it is a one-step process that includes two contributions: the LEM transition and the EMM transition. The observed anomalous redshifts, which cannot be explained by the free-electron model [35] and other theories [23–25], are attributed to the atomic binding potential and the momentum transfer from the incident photons to the electron during the collision. Our results have demonstrated that the redshift is a general phenomenon that can be observed in any scattering geometry. All these findings promote significantly the understanding of the nonlinear scattering processes of bound electrons in X-ray laser fields.

We thank all the members of SFAMP club for helpful discussions. SS thanks D. Krebs and M. Fuchs for helpful discussions. This work was supported by the National Natural Science Foundation of China under Grant Nos. 12074418, 11774411 and 11834015. ZCY was supported by the NSERC of Canada.

- 
- [1] P. Emma, R. Akre, J. Arthur, R. Bionta, C. Bostedt, J. Bozek, A. Brachmann, P. Bucksbaum, R. Coffee, F.-J. Decker, *et al.*, *Nat. Photon.* **4**, 641 (2010).
- [2] B. W. McNeil and N. R. Thompson, *Nat. Photon.* **4**, 814 (2010).
- [3] T. Ishikawa, H. Aoyagi, T. Asaka, Y. Asano, N. Azumi, T. Bizen, H. Ego, K. Fukami, T. Fukui, Y. Furukawa, *et al.*, *Nat. Photon.* **6**, 540 (2012).
- [4] P. R. Ribic and G. Margaritondo, *J. Phys. D: Appl. Phys.* **45**, 213001 (2012).
- [5] C. Bostedt, J. Bozek, P. Bucksbaum, R. Coffee, J. Hastings, Z. Huang, R. Lee, S. Schorb, J. Corlett, P. Denes, *et al.*, *J. Phys. B* **46**, 164003 (2013).
- [6] M. Altarelli, *High Power Laser Sci. Eng.* **3** (2015).
- [7] S. Shwartz, M. Fuchs, J. Hastings, Y. Inubushi, T. Ishikawa, T. Katayama, D. Reis, T. Sato, K. Tono, M. Yabashi, *et al.*, *Phys. Rev. Lett.* **112**, 163901 (2014).
- [8] K. Tamasaku, E. Shigemasa, Y. Inubushi, T. Katayama, K. Sawada, H. Yumoto, H. Ohashi, H. Mimura, M. Yabashi, K. Yamauchi, *et al.*, *Nat. Photon.* **8**, 313 (2014).
- [9] S. Ghimire, M. Fuchs, J. Hastings, S. C. Herrmann, Y. Inubushi, J. Pines, S. Shwartz, M. Yabashi, and D. A. Reis, *Phys. Rev. A* **94**, 043418 (2016).
- [10] L. Young, E. P. Kanter, B. Kraessig, Y. Li, A. March, S. Pratt, R. Santra, S. Southworth, N. Rohringer, L. DiMauro, *et al.*, *Nature (London)* **466**, 56 (2010).
- [11] M. Fuchs, M. Trigo, J. Chen, S. Ghimire, S. Shwartz, M. Kozina, M. Jiang, T. Henighan, C. Bray, G. Ndabashimiye, *et al.*, *Nat. Phys.* **11**, 964 (2015).
- [12] M. Cooper, *Adv. Phys.* **20**, 453 (1971).
- [13] P. Eisenberger and P. Platzman, *Phys. Rev. A* **2**, 415 (1970)
- [14] J. W. Du Mond, *Phys. Rev.* **33**, 643 (1929).
- [15] R. Ribberfors, *Phys. Rev. B* **12**, 2067 (1975).
- [16] P. Holm and R. Ribberfors, *Phys. Rev. A* **40**, 6251 (1989).
- [17] L. LaJohn, *Phys. Rev. A* **81**, 043404 (2010).
- [18] R. Pratt, L. LaJohn, V. Florescu, T. Surić, B. K. Chatterjee and S. Roy, *Radiat. Phys. Chem.* **79**, 124 (2010).
- [19] W. Ching and J. Callaway, *Phys. Rev. B* **9**, 5115 (1974).
- [20] D. Laurent, C. Wang, and J. Callaway, *Phys. Rev. B* **17**, 455 (1978).
- [21] P. Jaiswal and A. Shukla, *Phys. Rev. A* **75**, 022504 (2007).
- [22] B. Sankarshan and T. Umesh, *Radiat. Phys. Chem.* **144**, 106 (2018).
- [23] A. N. Hoppersky, A. M. Nadolinsky, and S. A. Novikov, *Phys. Rev. A* **92**, 052709 (2015).
- [24] D. Krebs, D. A. Reis, and R. Santra, *Phys. Rev. A* **99**, 022120 (2019).
- [25] A. Venkatesh and F. Robicheaux, *Phys. Rev. A* **101**, 013409 (2020).
- [26] D.-S. Guo, T. Åberg, and B. Crasemann, *Phys. Rev. A* **40**, 4997 (1989).
- [27] L. Gao, X. Li, P. Fu, R. Freeman, and D.-S. Guo, *Phys. Rev. A* **61**, 063407 (2000).
- [28] B. Wang, L. Gao, X. Li, D.-S. Guo, and P. Fu, *Phys. Rev. A* **75**, 063419 (2007).
- [29] B. Wang, Y. Guo, J. Chen, Z.-C. Yan, and P. Fu, *Phys. Rev. A* **85**, 023402 (2012).
- [30] F. Mackenroth and A. Di Piazza, *Phys. Rev. A* **83**, 032106 (2011).

- [31] D. Seipt and B. Kämpfer, Phys. Rev. A **83**, 022101 (2011).
- [32] A. Angioi, F. Mackenroth, and A. Di Piazza, Phys. Rev. A **93**, 052102 (2016).
- [33] M. Gell-Mann and M. Goldberger, Phys. Rev. **91**, 398 (1953).
- [34] R. Karazija, *Introduction to the Theory of X-ray and Electronic Spectra of Free Atoms* (Springer Science & Business Media, 2013).
- [35] L. S. Brown and T. Kibble, Phys. Rev. **133**, A705 (1964).